Limit cycle phase and Goldstone mode in driven dissipative systems

H. Alaeian,[1,2,*] G. Giedke,[3,4] I. Carusotto,[5] R. Löw,[1,2] and T. Pfau[1,2]

[1]*5th Institute of Physics, University of Stuttgart, Pfaffenwaldring 57, 70569 Stuttgart, Germany*

[2]*Center for Integrated Quantum Science and Technology (IQST), University of Stuttgart, Pfaffenwaldring 57, D-70550 Stuttgart, Germany*

[3]*Donostia International Physics Center, Paseo Manuel de Lardizabal 4, E-20018 Donostia-San Sebastian, Spain*

[4]*Ikerbasque Foundation for Science, Maria Diaz de Haro 3, E-48013 Bilbao, Spain*

[5]*INO-CNR BEC Center and Department of Physics, University of Trento, I-38123 Povo, Italy*

(Received 30 July 2020; accepted 21 December 2020; published 11 January 2021)

In this article, we theoretically investigate the first- and second-order quantum dissipative phase transitions of a three-mode cavity with a Hubbard interaction. In both types, there is a mean-field (MF) limit cycle phase where the local U(1) symmetry and the time-translational symmetry of the Liouvillian superoperator are spontaneously broken. In MF, this spontaneous symmetry breaking manifests itself through the appearance of an unconditionally and fully squeezed state at the cavity output, connected to the well-known Goldstone mode. By employing the Wigner function formalism, hence, properly including the quantum noise, we show that away from the thermodynamic limit and within the quantum regime, fluctuations notably limit the coherence time of the Goldstone mode due to the phase diffusion. Our theoretical predictions suggest that interacting multimode photonic systems are rich, versatile test beds for investigating the crossovers between the mean-field picture and quantum phase transitions, a problem that can be investigated in various platforms including superconducting circuits, semiconductor microcavities, atomic Rydberg polaritons, and cuprite excitons.

DOI: 10.1103/PhysRevA.103.013712

I. INTRODUCTION

For many decades, quantum phase transitions (QPTs) have been the subject of intense studies in several areas of physics [1]. In a closed system with unitary dynamics, the hallmark of an equilibrium QPT is the nonanalytic behavior of an observable upon changing a physical parameter [2–5]. In recent years, a new frontier has emerged in many-body physics, investigating nonequilibrium phase transitions. In that regard and as a suitable test bed, driven-dissipative quantum systems and their phase transitions have been the subject of many studies. Observation of exciton-polariton BEC in semiconductors [6,7] and cuprites [8] and their superfluidity [9,10], probing the first-order phase transitions, dynamical hysteresis, and Kibble-Zurek quench mechanism in microcavities [11,12], and demonstration of dynamical bifurcation and optical bistability in circuit QED [13–18] are a few examples of the rapidly growing body of experimental explorations of such physics in different platforms.

In parallel, some general aspects of nonequilibrium QPT have been investigated theoretically [19,20], and for specific systems such as coupled spins [21–23], interacting bosonic systems [24–27], and semiconductor microcavities [28]. Due to their coupling to a bath, driven-dissipative dynamics are not given by a Hermitian Hamiltonian but with a superoperator that supports a gapped mode at QPTs [29–31]. In spite of all the progress, a full theory of dissipative phase transition (DPT) has not yet been developed and the study of specific examples can aid this theoretical endeavor and hone the crossover between DPT and the phase transition in the thermodynamic limit (TD). Moreover, it can bring to the fore rich and various phenomena such as highly entangled states. Although due to their constant interaction with the environment, open systems are inherently far from the thermodynamic equilibrium, still there could be some parameter ranges where the system asymptotically approaches the mean-field (MF) limit, where quantum correlations and fluctuations can be ignored.

To be more specific, in this paper we focus our studies on a driven-dissipative three-mode bosonic system subject to Kerr-type intra- and intermodal interactions. To keep our results and discussions general, we do not specify the nature of the bosonic system. But let us remark that such setup could be realized in various platforms, including cavity Rydberg polaritons [32–34], excitons in 2D materials and semiconductors [35,36], microwave photons in superconducting circuits [37], and interacting photons in optical cavities [38].

Starting from the MF description we first explore the phase transitions of the system as a function of its parameters, i.e., pump, detuning, interaction strength, and bare-cavity mode spacing. We show that depending on the bare cavity features, the phase transition can be either continuous (2nd-order phase transition) or abrupt (1st-order phase transition) corresponding to an optical multistability, as studied for planar microcavities [39]. In both cases, the phase transition manifests itself by a nonzero amplitude of the unpumped modes and is related to the dissipative gap closure of the Liouvillian.

*Departments of Electrical & Computer Engineering, Purdue University, West Lafayette, IN 47907, USA; Department of Physics and Astronomy, Purdue University, West Lafayette, IN 47907, USA.

We show that within this range and up to the MF level, there is an unconditionally squeezed mode at the output, attributed to the spontaneous breaking of the local U(1) and time-translational symmetry (TTS). While in TD limit, the diverging quadrature of this state is related to the well-known, freely propagating Goldstone mode [40–42], employing the Wigner phase-space representation we show that within the quantum limit this mode is susceptible to fluctuations and becomes short lived. Since employing the Wigner formalism allows us to properly include the quantum noise, we have been able to explore the phase diagram more accurately and beyond MF. That also helps to delineate the validity range of MF when it comes to the study of QPT. In spite of its simplicity, the investigated system reveals important dynamics of driven-dissipative bosonic gases and could be a quintessential model for further exploration of spontaneous symmetry breaking (SSB) in open many-body systems.

The paper is organized as follows: In Sec. II we present the general problem, its MF description in the form of a generalized Gross-Pitaevskii equation (GPE), and the low-energy excitation spectrum determined via Bogoliubov treatment. We also summarize the stochastic formulation of the problem based on the truncated Wigner phase-space method. In Sec. III we present the numerical results of the three-mode cavity where various phase transitions are investigated and discussed. Finally, the last section summarizes the main results of the paper and sets the stage for future directions that can be explored in such systems.

II. PROBLEM FORMULATION

Consider a three-mode cavity with the following Hamiltonian describing the interaction dynamics between the modes $\hat{a}_{1,2,3}$,

$$\hat{H}_{ph} = \sum_{n=1}^{3}\left(\omega_m \hat{a}_m^\dagger \hat{a}_m + \frac{V_0}{2}\sum_{m}^{3}\hat{a}_m^\dagger \hat{a}_n^\dagger \hat{a}_m \hat{a}_n\right) + V_0\left(\hat{a}_2^{\dagger 2} a_1 a_3 + \hat{a}_1^\dagger \hat{a}_3^\dagger \hat{a}_2^2\right), \tag{1}$$

where ω_m is the frequency of the mth mode of the bare cavity and V_0 is the interaction strength. We would like to emphasize that the Hamiltonian could be the description of an exciton-polariton system or an optical parametric oscillator.

A coherent drive at frequency ω_L excites the pth mode of the cavity at the rate of Ω_0 as

$$\hat{H}_D = \Omega_0(\hat{a}_p e^{+i\omega_L t} + \hat{a}_p^\dagger e^{-i\omega_L t}). \tag{2}$$

Assuming a Markovian single-photon loss for the mode-bath coupling, the following Lindblad master equation describes the evolution of the reduced cavity density matrix $\hat{\rho}$ as

$$\frac{d\hat{\rho}}{dt} = -i[\hat{H}, \hat{\rho}] + \sum_m \gamma_m(2\hat{a}_m\hat{\rho}\hat{a}_m^\dagger - \{\hat{a}_m^\dagger\hat{a}_m, \hat{\rho}\}), \tag{3}$$

where $\hat{H} = \hat{H}_{ph} + \hat{H}_D$ on the right-hand side describes the unitary dynamics of the system and the second term captures the quantum jumps and losses of the mth-cavity field at rate γ_m.

Equivalently, we can derive the equations of motion for $\hat{a}_m$ operators and describe the dynamics via Heisenberg-Langevin equations as [43]

$$\dot{\hat{a}}_m = -i(\Delta_m - i\gamma_m)\hat{a}_m - iV_0\sum_{nkl}\eta_{kl}^{mn}\hat{a}_n^\dagger\hat{a}_k\hat{a}_l - i\Omega_0\delta_{mp} + \sqrt{2\gamma_m}\hat{\xi}_m(t), \tag{4}$$

where in the above equation $\Delta_m = \omega_m - \omega_L$ is the frequency of the mth mode in the laser frame, η_{kl}^{mn} is the mode-specific prefactor arising from different commutation relations, and $\{\hat{\xi}_m(t)\}$ describe stationary Wiener stochastic processes with zero means and correlations as

$$\langle\hat{\xi}_m^\dagger(t+\tau)\hat{\xi}_n(t)\rangle = n_{th}\delta(\tau)\,\delta_{mn}, \qquad \langle\hat{\xi}_m(t+\tau)\hat{\xi}_n^\dagger(t)\rangle = (1+n_{th})\delta(\tau)\,\delta_{mn}. \tag{5}$$

In the above equations, n_{th} is the number of thermal photons at the given temperature.

For numerical calculations, the dimension of the relevant (few-photon) Hilbert space grows rapidly with increasing number of modes and particle number. Hence, the direct solution of the density matrix in Eq. (3) is only possible for a small number of modes and at a low pumping rate Ω_0. For the quantum Langevin equations in Eq. (4), the two-body interaction generates an infinite hierarchy of the operator moments, making them intractable as well.

The most straightforward approach is a classical MF treatment where the correlations are approximated with the multiplication of the expectation values, i.e., $\langle\hat{a}_m\hat{a}_n\rangle \approx \langle\hat{a}_m\rangle\langle\hat{a}_n\rangle = \alpha_m\alpha_n$. These substitutions simplify the equations of motion of the operators' MFs in Eq. (4) to a set of coupled nonlinear equations as

$$i\dot{\alpha}_m = (\Delta_m - i\gamma_m)\alpha_m + V_0\sum_{nkl}\eta_{kl}^{mn}\alpha_n^*\alpha_k\alpha_l + \Omega_0\delta_{mp}. \tag{6}$$

Equation (6) is a Gross-Pitaevskii type equation with added drive and dissipation terms. In the steady state, the mean values are determined as $\dot{\alpha}_m = 0$. In this work, we use the Jacobian matrix to check the dynamical stability of all steady states.

Although the MF provides a good starting point, information about quantum correlations is lost. To improve this, we replace $\hat{a}_m = \alpha_m + \hat{b}_m$ and linearize Eq. (4) around MF determined from the steady state of Eq. (6). Defining $\hat{B} = [\hat{b}_1, \ldots, \hat{b}_N, \hat{b}_1^\dagger, \ldots, \hat{b}_N^\dagger]^T$ (superscript T stands for the transpose) as the fluctuation operator vector with $2N$ components, its time evolution is determined as

$$\frac{d\hat{B}}{dt} = M\hat{B} + D^{1/2}\hat{\Xi}, \tag{7}$$

where M is the Bogoliubov matrix at the MF α_m, $D = \mathrm{diag}(2\gamma_m)$, and $\hat{\Xi}$ is the noise operator vector of the Wiener processes in Eq. (4). As shown in Appendix A, from $\hat{B}$ one can directly determine the covariance matrix, $\mathrm{C}_B(\omega)$, whose entries are the stationary two-time correlations of the (zero-mean) operators $\hat{B}_i, \hat{B}_j$,

$$\Gamma_{ij}(\omega) = \mathcal{F}\left\langle\lim_{t\to\infty}\hat{B}_i(t+\tau)\hat{B}_j(t)\right\rangle = \langle\tilde{\hat{B}}_i(\omega)\tilde{\hat{B}}_j(-\omega)\rangle\,, \tag{8}$$

where $\mathcal{F}$ represents the Fourier transform of the correlation with respect to to the delay τ, and $\tilde{\hat{B}}_i(\omega)$ is the Fourier transform of $\hat{B}_i(t)$.

Within the Born-Markov approximation, if the 2nd-order dynamics is contractive and in the vicinity of the steady state it dominates over the higher-order terms, then most of the important correlations can be obtained from the linearized Bogoliubov treatment as in Eq. (7). This is a self-consistent criterion with M having a spectrum with negative real parts, and is typically satisfied at large particle numbers and weak interactions, as for the TD limit, where MF treatment is well justified.

To examine the validity of the MF and linearization in the quantum limit of a small number of particles, we further employ the Wigner function (WF) representation to express the system dynamics in terms of the analytic quasiprobability distribution $W(\vec{\alpha};t)$ [43,44]. While the complete dynamics of the Wigner function exactly reproduces the quantum dynamics, the presence of the third-order derivative terms in the time evolution of $W(\vec{\alpha};t)$ makes the complete simulation numerically intractable. The truncated Wigner dynamics that originates from discarding the third-order derivative terms results in a numerically efficient and stable Fokker-Planck equation. Using Itô calculus, it can be further mapped to a set of stochastic differential equations (SDEs) for α_m with the following general form [45] (more details can be found in Appendix B):

$$d\alpha_m = A_m dt + \sum_{m'} D_{m,m'}\, dN_m, \tag{9}$$

where dN_m is a complex Wiener process describing a Gaussian white noise.

Within the Wigner approach, the expectation value of any symmetrically ordered operator $\hat{O}_{sym}$, which is formed by an equally weighted average of all possible orderings of the underlying bosonic operators $\hat{a}_m$ and $\hat{a}_m^\dagger$ at time t, can be obtained as

$$\langle \hat{O}_{sym}(t)\rangle = \langle\langle O_{sym}(t)\rangle\rangle\,, \tag{10}$$

where $\langle\langle . \rangle\rangle$ indicates the average over the trajectories of the stochastic equation. The expectation values of generic operators, e.g., normally ordered ones, are then straightforwardly obtained taking into account the bosonic commutation rules between the $\hat{a}_m$ and $\hat{a}_m^\dagger$ operators.

Before leaving this section, we would like to emphasize that the beyond-MF corrections of GPE in Eq. (6) need the effect of the 2nd and the 3rd normally and anomalously ordered correlations. These terms contribute to the MF as *state-dependent* noises. In the truncated Wigner function (TWF) method, there are additional drift terms as well as Langevin forces to capture those aforementioned quantum-field corrections, partially. While the full dynamics of $W(\vec{\alpha};t)$ in Eq. (B6) is equivalent to the master equation in Eq. (3), the TWF is an approximation which can only be applied to initially positive WF and preserves this property. It can be interpreted as the semiclassical version of Langevin equations of Eq. (4). Thus, the TWF and its equivalent SDE in Eq. (9) might not be able to reproduce the quantum dynamics fully. However, it goes beyond the MF-Bogoliubov treatment and can describe the generation of non-Gaussian and nonclassical states [46].

III. RESULTS AND DISCUSSION

Throughout this section we assume identical field decay rates for all cavity modes, i.e., $\gamma_m = \gamma_0$, and express all other rates normalized to this value. Similarly, time is expressed in units of γ_0^{-1}. A coherent drive as in Eq. (2) excites the second mode, i.e., $\hat{a}_2$. Hence, the 1st and 3rd modes are populated equally (more discussions can be found in Appendix A). Thermal fluctuations due to the bath are assumed to be zero, i.e., $n_{th} = 0$. Part of the full quantum mechanical calculations is done with QuTip open-source software [47,48]. The numerical convergence in each case has been tested by increasing the number of random initializations (MF), random trajectories (SDE), and the truncation number in Fock states (density matrix) to have a relative error $\lesssim 10^{-5}$ in the particle number.

In a driven-dissipative system, the interplay between coherent excitation rate and its detuning, incoherent loss, and interaction leads to notable changes in system properties, typically known as dissipative phase transition. In the multimode case we consider here, we have an additional important parameter governing the DPT, namely $\delta_D = 2\omega_2 - (\omega_1 + \omega_3)$, which is the anharmonicity of the bare cavity. We call the cavity *harmonic* if $\delta_D = 0$ and *anharmonic* otherwise. Note that harmonic and anharmonic do not refer here to the deviations from bosonicity or the nonlinearity of the field dynamics, which is encoded in the V_0 parameter, but rather to the spatial shape of the external potential acting on photons and giving rise to the spectrum of cavity modes.

Similar phase diagrams and multistability phenomena have been studied for exciton-polaritons in planar cavities where δ_D vanishes [39]. However unlike the planar case where a continuum of modes is available, here the frequencies of the generated pairs are set by the bare cavity modes and the interaction, self-consistently. Note that we are focusing here on cavity configurations, to be distinguished from running-wave optical parametric oscillators for which different phase-matching conditions apply [49].

Figures 1(a), 1(b) show the phase diagram of a harmonic cavity as a function of the interaction strength V_0 and the laser detuning Δ_0, respectively. The phase diagram closely resembles the DPT of a single-mode cavity depicted in Figs. 11(a), 11(b) in Appendix C. While it is in the (Π_1) phase, i.e., the yellow region, the pumped mode has one stable stationary state.

In the (Π_2) phase, i.e., the orange region, there are two distinct values for the pumped mode. Finally, in the (Π_3) phase, i.e., the red region which only appears in the multimode case, the system is within a tristable phase and the pumped mode has three stable MF stationary states. In Fig. 2 we plot $\langle \hat{n}_{1,2}\rangle$ for $V_0 = 0.1, 1$ at $\Delta_0 = -3$ as a function of the pumping rate varied along the dotted lines (I), (II) in Figs. 1(a), 1(b) respectively. There, the black lines show all the MF solutions determined from Eq. (6). However, not all of the solutions are stable in terms of the elementary excitation spectrum. As mentioned in the previous section, we determine the stable branches based on the Bogoliubov matrix eigenvalues. In each panel, the solid black lines show the stable solutions and the dashed black lines indicate the unstable branches. The stable solutions can be determined directly via integrating the coupled equations of motions for the MF. The purple line with

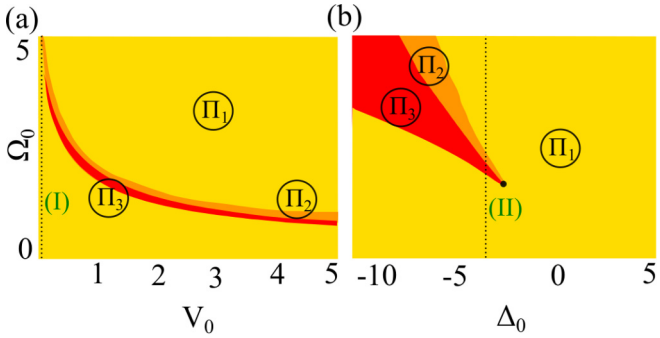

FIG. 1. MF dissipative phase diagram of a three-mode harmonic cavity, i.e., $2\omega_2 = \omega_1 + \omega_3$, as a function of (a) the interaction strength V_0 and (b) the laser detuning Δ_0. In each panel the yellow (Π_1), orange (Π_2), and red (Π_3) regions correspond to the presence of one, two (bistability), and three stable (tristability) stationary states for the pumped mode, respectively. In (a) the detuning is fixed at $\Delta_0 = -3$ and in (b) the interaction strength has the constant value $V_0 = 1$. The dotted vertical lines [labeled (I) and (II)] at $V_0 = 0.1$ and $\Delta_0 = -3$ indicate the cuts through the phase diagram studied in subsequent figures. Rates are in units of γ_0.

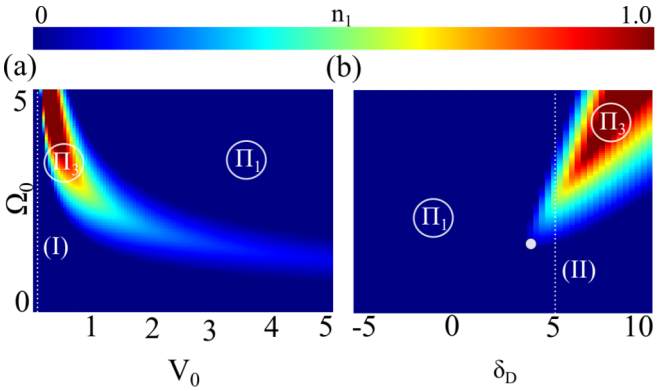

FIG. 3. Number of photons in the 1st, 3rd modes of a three-mode anharmonic cavity ($2\omega_2 \neq \omega_1 + \omega_3$), as a function of the (a) interaction strength V_0 and (b) anharmonicity δ_D, determined from MF, where all rates are in units of γ_0. In (a) $\delta_D = 5$ and in (b) $V_0 = 1$ and the laser is always resonantly pumping the 2nd mode $\Delta_0 = 0$. (Π_1), (Π_3) indicate two different phases of zero and nonzero population of the first mode. The dotted vertical lines [labeled (I) and (II)] at $V_0 = 0.1$ and $\delta_D = 5$ indicate the cuts through the phase diagram studied in subsequent figures.

diamonds shows the data calculated using the SDE method averaged over 2000 random trajectories, and the solid red line in panels (c), (d) depicts the results of the full density matrix (DM) calculations as a benchmark. It can be seen that the phase transitions are discontinuous, i.e., a *first-order* PT. Moreover, for all modes the difference between stable MF branches decreases upon increasing the interaction from $V_0 = 0.1$ to $V_0 = 1$ in Figs. 2(a), 2(b) and Figs. 2(c), 2(d) respectively. Aside from the finite region around the multistability, also it can be seen that the results of MF, SDE, and DM agree quite well (note a similar tendency for the single-mode case in Fig. 12 of Appendix C). For the 1st mode on the other hand, both Figs. 2(a) and 2(c) indicate that the finite MF tristable region (Π_3 in the DPT) is the only parameter range where this mode gets a nonzero amplitude.

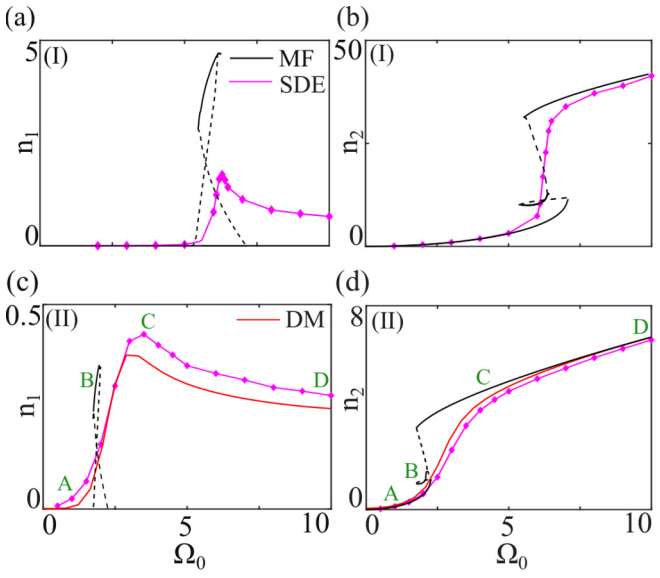

FIG. 2. Population of the 1st and the 2nd mode in a harmonic cavity, i.e., $\delta_D = 0$, as a function of the pumping rate Ω_0 calculated from MF (solid black lines for stable and dashed lines for unstable solutions) and SDE (purple diamonds). Solid red line in panels (c), (d) show the density matrix solutions for comparison. $V_0 = 0.1$ in panels (a), (b) and $V_0 = 1$ in (c), (d). In both cases $\Delta_0 = -3$ and all rates are normalized to γ_0.

As already mentioned, the QPT of a harmonic cavity and of a single-mode cavity are very similar and, as can be seen from comparing Fig. 1 and Fig. 11, the multimode tristability region is a subset of the single-mode bistability region. In other words, the multistability is a necessary but not sufficient condition for having the parametric pair generation of unpumped modes. To establish a physical qualitative picture, one can consider the symmetric sidebands generated due to the self-interacting cavity mode (Fig. 13). These sidebands are always generated due to the pumped mode and in a multimode cavity they overlap with the unpumped modes hence behaving as excitation for them. When the pumping rate due to these sidebands exceeds the linewidth of the mode, i.e., the cavity decay rate, one can get nonzero MF amplitude for the unpumped modes as well. By populating those modes their self-interaction becomes important as well and they start to move out of resonance. Hence the pumping rate via the sidebands decreases, and the MF amplitude of these modes vanishes again; i.e., the parametric process stops. That explains why one has a finite region of nonzero values for the 1st and 3rd modes as shown in Figs. 2(a), 2(c).

The situation is different in an anharmonic cavity where $\delta_D \neq 0$. Figures 3(a), 3(b) show the average number of photons in unpumped modes $\langle \hat{n}_{1,3} \rangle$ as a function of the interaction strength V_0, the pumping rate Ω_0, and the anharmonicity parameter δ_D. For better illustration, in Figs. 4(a), 4(b) and Figs. 4(c), 4(d) we plot the average number of photons in all cavity modes as a function of the pump rate at weak ($V_0 = 0.1$) and strong ($V_0 = 1$) interaction, respectively, when the pumping rate is continuously increased along the (I) and

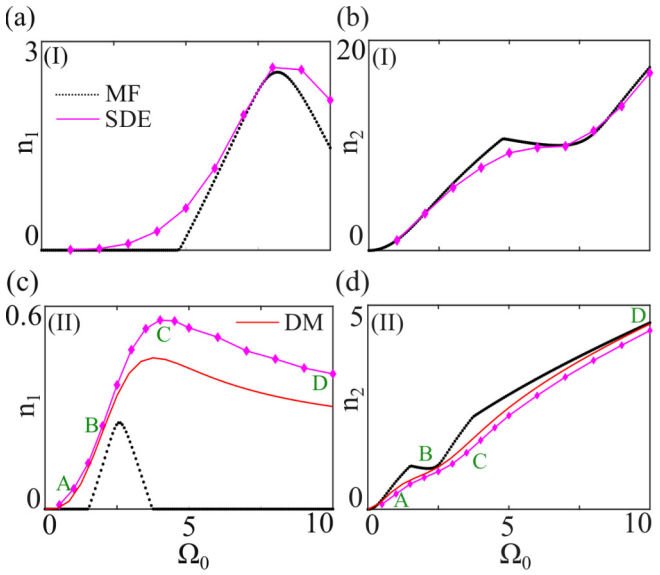

FIG. 4. Population of the 1st (3rd) and the 2nd mode, in an anharmonic cavity with $\delta_D = 5$, as a function of the pumping rate (Ω_0) calculated from MF (black dots), SDE (purple diamonds). Solid red line in panels (c), (d) shows the DM solutions for comparison. $V_0 = 0.1$ in panels (a), (b) and $V_0 = 1$ in (c), (d). In both cases $\Delta_0 = 0$ and the rates are normalized to γ_0.

(II) dotted lines in Figs. 3(a), 3(b). Unlike the harmonic cavity case, here we only have two phases (Π_1), (Π_3), where the transition occurs continuously (but is nonanalytic), i.e., in a *second-order* PT, with a unique-valued order parameter in each phase.

As elaborated in Appendix A, for the single-mode cavity, the interaction of the pumped mode (2nd mode here) with itself creates energetically symmetric sidebands. In a multimode case, the interplay between the intra- and intermode interactions leads to the excitation of other modes both in the harmonic as well as anharmonic cavities. Similarly for both, MF predicts a threshold and a finite parameter range for nonzero amplitude of the 1st mode. While the lower threshold is set solely by the pumped mode when $V_0 n_2 \geqslant \gamma_2$, the upper threshold is dependent on the population of the other two modes as well as their relative energies. (The lowest and highest pumping rate is set by the constraints on Φ_0, Φ_p, respectively, as detailed in Appendix A.)

When quantum fluctuations are included, however, either via SDE or full density matrix (DM) calculations, a unique, continuous, and nonzero solution for all three modes is predicted at all pumping rates. In both cavities and for the pumped mode, MF, SDE, and DM results agree quite well in (Π_1) phase. For the parametrically populated modes however, the SDE and DM results are in good agreement over the whole range but are remarkably different from MF. However, the rising slope of the former analyses always coincides with the transition to the MF (Π_3) phase.

Spontaneous symmetry breaking and Goldstone mode

In the absence of the coherent pump, the Liouvillian superoperator $\mathcal{L}$ of Eq. (3) has a continuous global U(1) symmetry,

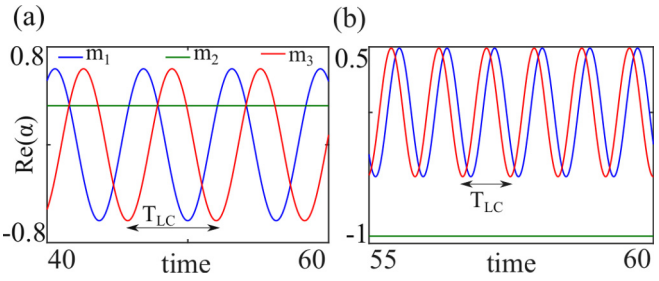

FIG. 5. Temporal behavior of the mean fields $\alpha_j(t)$ within the MF (Π_3) phase in a three-mode (a) harmonic cavity at $\Omega_0 = 1.85$, $\Delta_0 = -3$ and (b) anharmonic cavity at $\Omega_0 = 2$, $\delta_D = 5$, and $V_0 = 1$. In both panels the blue, green, and red lines correspond to the 1st, 2nd, and 3rd mode, respectively. The time is in units of γ_0^{-1}, and T_{LC} indicates the limit-cycle period.

which is broken by a coherent drive of Eq. (2). However, with the Hamiltonian of Eq. (1) for the three-mode cavity, $\mathcal{L}$ still has a local U(1) symmetry as it remains unchanged under the following transformations for any arbitrary phase Θ_0 [40]:

$$\hat{a}_1 \to \hat{a}_1 e^{+i\Theta_0}, \ \hat{a}_3 \to \hat{a}_3 e^{-i\Theta_0}. \tag{11}$$

If the MF amplitudes $\alpha_{1,3} = 0$, then the steady state respects the Liouvillian's symmetry and can be unique. However, for $\alpha_{1,3} \neq 0$ as occurs within the (Π_3) phase, the MF solutions are not U(1)-symmetric anymore. Hence, there is a *spontaneous symmetry breaking* (SSB) accompanied by a DPT. However, it is evident that the set of all solutions is invariant under the aforementioned rotations. In other words, within the (Π_3) phase there is a continuum of MF stationary states.

Figures 5(a), 5(b) show the typical temporal behavior of the order parameters α_m within the MF (Π_3) phase of the harmonic and anharmonic cavities, respectively. As can be seen, while the pumped mode m_2 is time invariant (green line), the parametrically populated modes $m_{1,3}$ (blue and red lines) show self-sustained oscillations with a random relative phase, reflecting the value the U(1) phase acquires in the SSB.

In the frame rotating with the laser, the Liouvillian $\mathcal{L}$ is TTS, which indeed is the symmetry of the solutions within the (Π_1), (Π_2) phase. Within the (Π_3) phase, however, the order parameter becomes time periodic and thus breaks the time-translational symmetry. Therefore, in both of the harmonic and anharmonic cavities, the MF (Π_3) phase is accompanied by SSB of the local U(1) symmetry and the TTS. This oscillatory behavior, known as the *limit-cycle* (LC) phase, is a clear distinction of DPT from its equilibrium counterparts [50–52]. From Fig. 5, the LC period can be determined as $T_{LC} \approx 6.28$ and $T_{LC} \approx 0.83$, corresponding to $\omega_{LC} = 1, 7.5$ for the harmonic and anharmonic cavities, respectively. These frequencies agree with the theoretical predictions of $\tilde{\Delta}_{1,3}$ in Appendix A.

The SSB of this continuous symmetry can be interpreted in terms of the gapless *Goldstone* mode. The eigenvalues $\{\lambda\}$ of the Bogoliubov matrix M in Eq. (7) directly determine the excitation energies around a MF stationary state, with $\mathrm{Re}(\lambda)$ being the excitation linewidth and $\mathrm{Im}(\lambda)$ its frequency. It is straightforward to check that due to the relative-phase freedom of the unpumped modes, M has a kernel along the

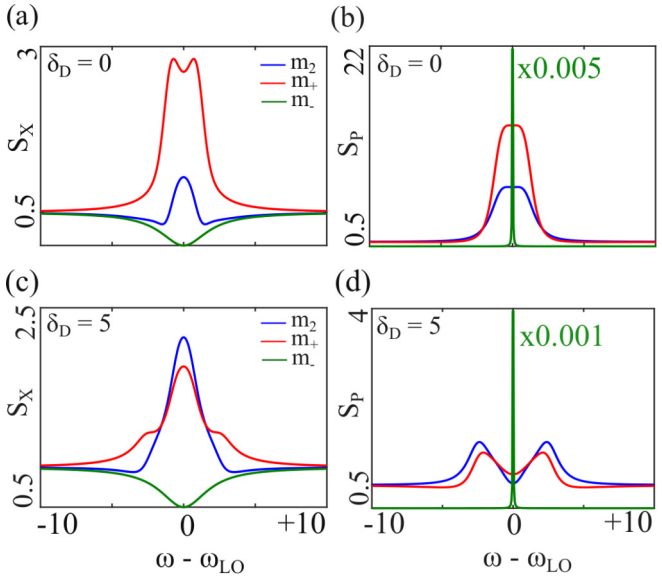

FIG. 6. Output X, P spectra of the modes in the (a), (b) harmonic cavity at $\Delta_0 = -3$, $\Omega_0 = 1.85$, and (c), (d) anharmonic cavity at $\Delta_0 = 0$, $\Omega_0 = 2$, calculated from the MF-Bogoliubov. In each panel the solid blue, red, and green lines correspond to the spectrum of the pumped (m_2), symmetric (m_+), and antisymmetric (m_-) modes, respectively. Due to its divergence, the momentum of the antisymmetric mode is scaled down in panels (b), (d). The frequency axis is in units of γ_0.

following direction [40] (more information is in Appendix A):

$$G = [\alpha_1, 0, -\alpha_3, -\alpha_1^*, 0, \alpha_3^*]^T, \tag{12}$$

where T means the transpose.

$\lambda_G = 0$ implies that in the local oscillator's frame, G is a zero energy mode ($\omega = 0$) with zero linewidth, i.e., an undamped excitation. To investigate the implications of this mode on quantum correlations, we employ Eq. (7) to calculate the X, P-quadrature spectra of the cavity output. Figure 6 shows the quadrature correlations of the output 2nd mode and ($m_\pm \propto m_1 \pm m_3$), i.e., the symmetric and antisymmetric superpositions of the two unpumped modes. Panels (a), (b) show the spectra of the harmonic cavity at $\Omega_0 = 1.85$, and panels (c), (d) show the same quantities for an anharmonic cavity at $\Omega_0 = 2$, which correspond to the point B within the MF LC phase, and on the rising slope of the SDE and DM results in Fig. 2(c) and Fig. 4(c). Although the spectral features of the pumped and the symmetric mode depend on detailed cavity features, the antisymmetric mode quadratures in harmonic and anharmonic cavities look alike [solid green lines in Figs. 6(c), 6(d)]. While S_{X_-} is always fully squeezed at the origin, the spectrum of its conjugated variable S_{P_-} diverges. From Eq. (12) it is clear that S_{P_-} is indeed the spectrum of the gapless Goldstone mode. Since in the MF picture this mode encounters no restoring force, its fluctuation diverges. (The analytic form of the spectra and further information can be found in Appendix A.)

To examine the robustness of the Goldstone mode and the consequent unconditional squeezing, we employ the SDE to study the beyond-MF behavior of the cavity state. Figure 7 shows the number state occupation probability (p_n) and the

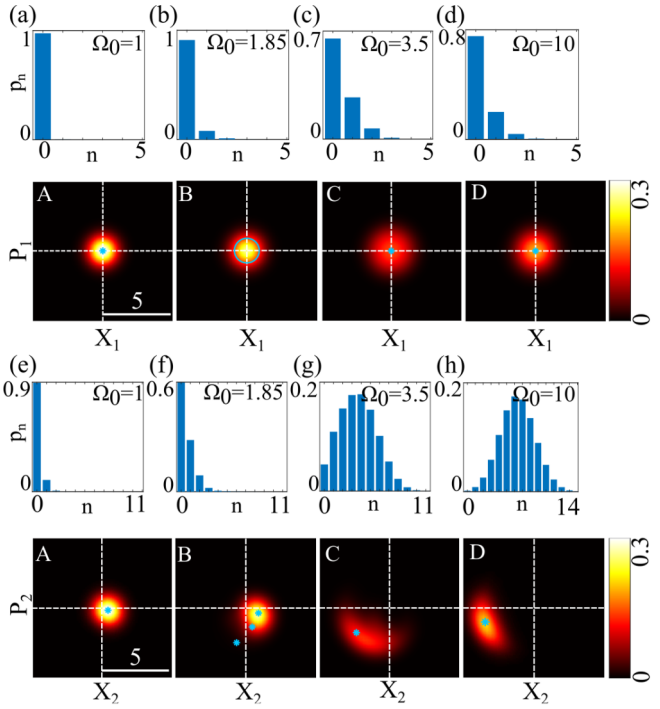

FIG. 7. Histograms of number state occupation probability p_n and color maps of the Wigner function of the (a)–(d) 1st mode and (e)–(h) 2nd mode, in a three-mode harmonic cavity when $\Delta_0 = -3$, $V_0 = 1$ for different pumping rates Ω_0 highlighted as (A, B, C, D) in Figs. 2(c), 2(d). In each phase-space map the white dashed lines show the axes ($X = 0$, $P = 0$) in the XP plane and the light blue stars or circles correspond to the predicted MF.

Wigner function distribution of the harmonic cavity at four different pumping rates $\Omega_0 = 1$, 1.85, 3.5, 10 corresponding to the (A, B, C, D) points in Fig. 2 at $V_0 = 1$, respectively. Panels (a)–(d) show these quantities for the 1st mode and panels (e)–(h) show the ones for the 2nd mode. As can be seen in all panels (a)–(d), distributions of the 1st mode are azimuthally symmetrically independent of the pumping rate, which is consistent with the local U(1) symmetry of the unpumped modes and their phase freedom, i.e., $\langle \hat{a}_{1,3} \rangle = 0$.

Within the (Π_1) phase at low pumping rate and before the parametric threshold, MF predicts zero amplitude for the 1st mode, while the 2nd mode looks like a coherent state [Figs. 7(a), 7(e)]. As the pumping rate increases [point B in Figs. 2(c), 2(d)], the system enters the LC phase in which mode 2 has three stable stationary states, as shown with three stars in Fig. 7(f), and the unpumped modes acquire a finite amplitude. The black circle in Fig. 7(b) shows the loci of MF stationary states. For larger values of the pump, close to the upper threshold of the multistability region [point C in Figs. 2(c), 2(d)], the system transitions to the uniform (Π_1) phase again where the 2nd mode attains a unique stationary state and the 1st mode has zero MF. However, as can be seen in Fig. 7(g) the cavity state is far from coherent due to the larger interaction at this photon number.

At even larger pumping rate shown in Figs. 7(d), 7(h) corresponding to the point D in Figs. 2(c), 2(d) [far within the (Π_1) phase], the 2nd mode is a non-Gaussian state whose phase-space distribution is reminiscent of the single-mode

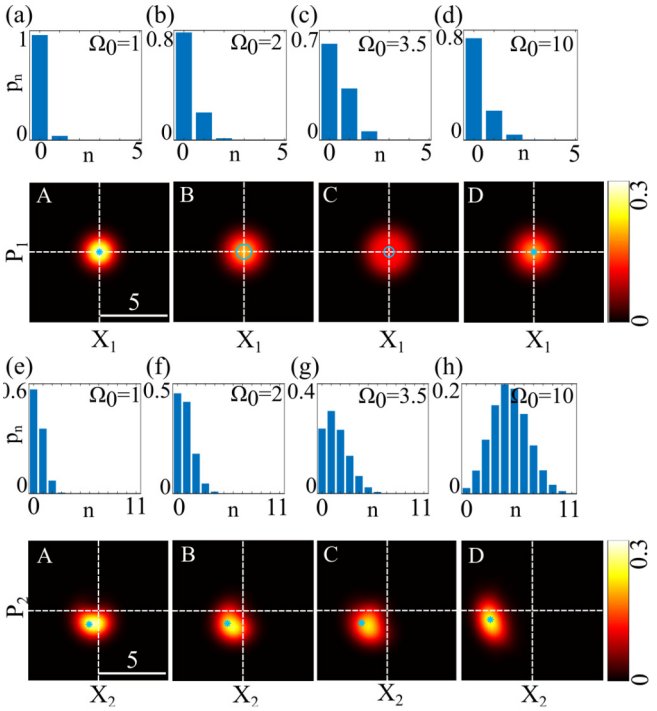

FIG. 8. Histograms of the number state occupation probability p_n and color maps of the Wigner function of the (a)–(d) 1st mode and (e)–(h) 2nd mode in a three-mode anharmonic cavity when $\Delta_0 = 0$, $\delta_D = 5$ and at $V_0 = 1$ for different pumping rates Ω_0 highlighted as (A, B, C, D) in Figs. 4(c), 4(d). In each phase-space map the white dashed lines show the axes ($X = 0, P = 0$) in the XP plane and the light blue stars or circles correspond to the predicted MF steady-state amplitudes.

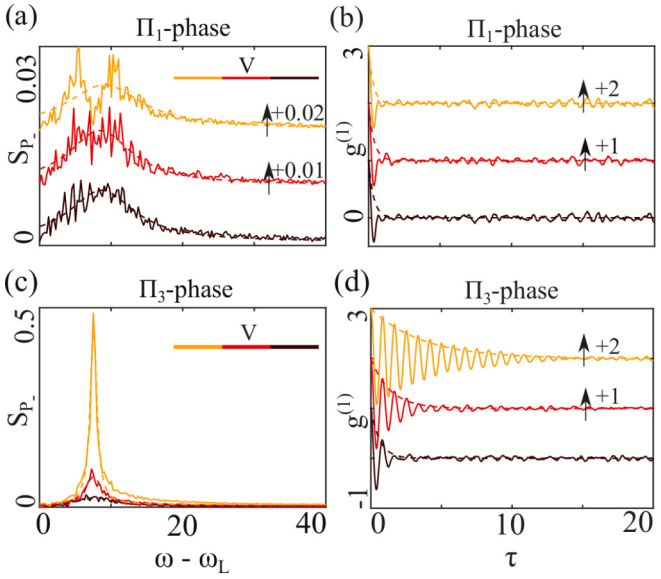

FIG. 9. SDE calculations of the (a), (c) spectral density in the laser frame (in units of γ_0) and (b), (d) delayed temporal correlation of P quadrature of in-cavity m_- mode in an anharmonic cavity. The upper row shows the behavior in the (Π_1) phase and the lower row shows that with the MF LC phase. The interaction is changed from $V_0 = 0.1$ to $V_0 = 0.5$ to $V_0 = 1.0$, yellow to red to brown, respectively. The dashed lines show the Lorentzian fit in (a), (c) and the exponential fits in (b), (d).

cavity in this regime (Fig. 12 of Appendix C). Also it is worth mentioning that in spite of the similar symmetric distribution of the 1st mode and its vanishing mean, its variance clearly changes as the system traverses the different phases.

For completeness, in Fig. 8 we detail the state of the anharmonic cavity through its different phases at four pumping rates of $\Omega_0 = 1, 2, 3.5, 10$ corresponding to (A, B, C, D) points in Figs. 4(c), 4(d). As can be seen the overall behavior of the cavity modes looks like that of the harmonic case, with the main distinction of always having one unique MF stationary state.

To study the robustness of the Goldstone mode in the presence of quantum fluctuations, from SDE analysis we calculate the correlation and spectrum of in-cavity $\hat{P}_-$ as

$$g^{(1)}(\tau) = \langle \lim_{t\to\infty} \hat{P}_-(t+\tau)\hat{P}_-(t)\rangle\,, \tag{13}$$

$$S_{P_-}(\omega) = \mathcal{F}(g^{(1)}(\tau)), \tag{14}$$

where $\hat{P}_- = i(\hat{a}_- - \hat{a}_-^\dagger)/\sqrt{2}$ is the momentum of the m_- mode. When using SDE trajectories to calculate such correlations, we are making a semiclassical assumption to evaluate the two-time operators replacing them with classical quantities and neglecting commutators [45].

The results are shown in Fig. 9 when the interaction V_0 is increased from 0.1 to 1 (brown to yellow lines). Panels (a), (b) are the spectra and correlations in the (Π_1) phase while (c), (d) are within the (Π_3) phase where LC is predicted by MF. For direct comparison with LC oscillations of Fig. 5(b) and highlighting ω_{LC}, the spectral densities in (a), (c) are shown in the laser (ω_L) frame, directly. Defining a dimensionless parameter N where $V_0 = V/N \to 0^+$ is the TD limit, the pumping rate is scaled by $\sqrt{N}$, so that $V_0\Omega_0^2$ is kept fixed. That way one can make the interaction per particle small (TD) but at the same time still have the same total interaction.

As can be seen in Figs. 9(a), 9(b) the observables are almost unchanged when the system is in the (Π_1) phase, where MF predicts zero amplitude for m_-. From Fig. 9(a) we can see that S_{P_-} is very small with a large linewidth (note that the data for $V_0 = 0.5, 0.1$ are shifted upward to provide clarity). Similarly, the temporal behavior in panel (b) shows a short correlation time.

On the contrary, when the system transitions to the MF LC phase by virtue of increasing the pumping rate, the spectral densities shown in Fig. 9(c) increase and an apparent resonance feature appears that becomes more prominent at weaker interaction closer to the TD limit, hence, the validity range of MF.

Similarly the temporal correlations in panel (d) show prolonged coherence times that increase at weaker interaction. To quantify these features better, we fit a Lorentzian line shape with the following form to $S_{P_-}(\omega)$:

$$L(\omega) = \frac{a}{(\omega - \omega_{\text{peak}})^2 + \Gamma^2} + c. \tag{15}$$

The fits are shown with dashed lines in Figs. 9(a), 9(c) and the center and linewidth fit parameters are presented in Table I. Within the (Π_1) phase, ω_{peak} and Γ slightly change

TABLE I. The Lorentzian fit parameters to the spectral density of P_- quadrature within the MF (Π_1) and (Π_3) phase as in Figs. 9(a), 9(c). All rates are in terms of γ_0.

	$V_0 = 0.1$	$V_0 = 0.5$	$V_0 = 1.0$
ω_{peak} (Π_1)	8.7	8.5	9
ω_{peak} (Π_3)	7.5	7.7	7.9
Γ (Π_1)	5.6	5.4	6.5
Γ (Π_3)	0.4	1.7	3.2

with the interaction V_0. Throughout the LC phase, on the other hand, $\omega_{\text{peak}} \approx 7.5$, i.e., the LC oscillation frequency ω_{LC} in Fig. 5(b). Moreover, starting from a narrow resonance ($\Gamma \approx 0.4$) at weak interaction (large N), the linewidth clearly increases ($\Gamma \approx 3.2$) by increasing the interaction (small N). Similar values were obtained by fitting the correlation functions with exponential functions, i.e., the dashed lines in Figs. 9(b), 9(d) independently.

Finally, we study the behavior of the P_--quadrature linewidth for the whole quantum-to-TD-limit transition, i.e., from small to large N. The results are depicted in Fig. 10 with red squares. The solid red line is the number of particles in this mode (right y axis), and the the solid blue line is a power-law fit to the data, indicating the linewidth narrowing scales as $N^{-0.9\pm0.03}$. In other words, while the gapless Goldstone mode picture in the TD limit (kernel of MF-Bogoliubov matrix) is corroborated well by a small $\Gamma \approx 0$ of the P_- quadrature for large N, approaching the quantum limit the decay rate notably increases due to the phase diffusion. It is worth comparing this tendency with the Schawlow-Townes laser linewidth scaling as N^{-1} [53].

To investigate the m_--mode noise spectra as well, we show the Wigner function distribution of this mode at a few different interaction points. As can be seen at larger N (point C), hence the weaker interaction, the phase-space distribution resembles the one of an X-squeezed state. However, upon increasing the interaction (points A, B) the squeezing decreases. This clearly confirms the phase diffusion effect in reducing the coherence time of the generated pairs. Besides, this effect becomes more dominant deep into the quantum range where the fluctuations should not be ignored.

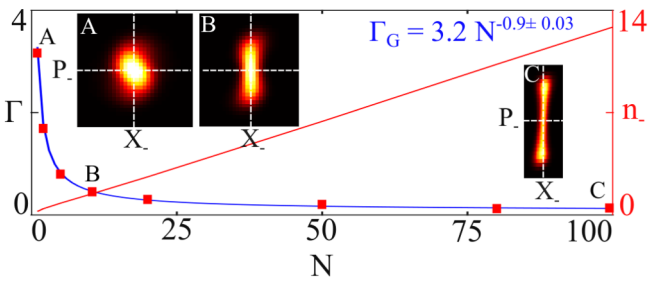

FIG. 10. The linewidth of the P_- quadrature (in units of γ_0), i.e., the Goldstone mode, within the MF LC phase as a function of the dimensionless parameter N. The red squares are the SDE calculation results while the solid blue line is a power-law fit to the data. The solid red line shows the average number of particles in this mode (right axis). The inset color maps show the TWF distribution of the m_- mode at a couple of interaction strengths.

IV. CONCLUSIONS

Exploring dissipative phase transitions is one of the important topics of open quantum systems. There, the interplay between dissipation, drive, and interaction can lead to a rich test bed to investigate dynamics of many-body systems far from their equilibrium. Among the interesting features that can be studied in these systems are the generation of steady-state many-body correlations, the sharp dependence of system parameters with applications in metrology, and the emergence of classical properties in quantum systems. In this article, we theoretically investigate the first- and second-order quantum dissipative phase transitions of in a three-mode cavity with intra- and intermodal two-body interaction as a prototypical model. We showed the emergence of a MF limit-cycle phase where the local U(1) symmetry and the TTS of the Liouvillian are spontaneously broken. We explained the connection between this phase and the Goldstone mode well studied in the TD limit. Including the effect of quantum noise by employing the truncated Wigner function formalism, we showed the breakdown of MF predictions within the quantum regime. Within this range, fluctuations notably limit the coherence time of the Goldstone mode due to the phase diffusion.

Concerning the experimental realizations, the model and the results are applicable to a wide variety of driven-dissipative interacting bosonic platforms, including circuit QED, semiconductor excitons, and multimode cavities with cold atoms [32,54], where the figure of merit V_0/γ can be tuned properly. It is also interesting to explore the feasibility of using such platforms in creating non-Gaussian states as an instrumental ingredient for quantum information protocols based on continuous variable entanglement and photonic quantum logic gates [15,55–57].

ACKNOWLEDGMENTS

The authors thank Wolfgang Schleich, Hans-Peter Büchler, Jan Kumlin, and Jens Hertkorn for insightful discussions. The invaluable IT support from Daniel Weller is greatly acknowledged. H.A. acknowledges financial support from the IQST Young Researchers grant and the Eliteprogram award of Baden-Württemberg Stiftung. I.C. acknowledges financial support from the European Union FET-Open grant "MIR-BOSE" (No. 737017), from the H2020-FETFLAG-2018-2020 project "PhoQuS" (No. 820392), and from the Provincia Autonoma di Trento.

APPENDIX A: COVARIANCE MATRIX FROM MF-BOGOLIUBOV

As described in the main text, the equations of motion for the vector of fluctuation operators $\hat{B} = [\hat{b}(t)]$ are given by the linearized Eq. (7). From this equation we can determine directly the Fourier transform of fluctuation operator $\hat{B}$ for the inside-cavity fields as

$$\hat{B}(\omega) = -(i\omega I + M)^{-1} D^{1/2} \hat{\Xi}(\omega), \tag{A1}$$

where ω is the frequency in the local oscillator (ω_{LO}) rotating frame. For dynamically stable solutions, i.e., for the real part of the spectrum of M being negative-definite, the above solution always exists. We define the following covariance matrix

spectrum with entries as in Eq. (8),

$$C_B^{(in)}(\omega) = \langle \hat{B}(\omega)\hat{B}^\dagger(-\omega)\rangle = \langle \hat{B}(\omega)\hat{B}(\omega)^\dagger\rangle$$
$$= (i\omega I + M)^{-1} D^{1/2} \langle \hat{\Xi}(\omega)\hat{\Xi}^\dagger(-\omega)\rangle$$
$$\times D^{1/2}(i\omega I + M)^{-1^\dagger},$$

where the superscript (in) refers to the inside-cavity fields, and the subscript B emphasizes the operators. $\langle \hat{\Xi}(\omega)\hat{\Xi}^\dagger(-\omega)\rangle$ is the noise spectral density, solely dependent on bath features, e.g., thermal photons density in our case. The coupling rate of the in-cavity field with the surrounding bath is captured via the matrix D. Other detailed information about the bare cavity modes, pumping, and interactions are contained in the matrix M. At any stable MF, the spectrum of M has negative real parts, so $C_B^{(in)}(\omega)$ is a well-defined quantity over the whole spectrum except $\omega = 0$, in the case where M has a kernel.

Employing the input-output formalism the output-field covariance matrix can be determined directly from $C^{(in)}(\omega)$. For a single-sided cavity we have

$$\hat{B}_{\text{out}} = D^{1/2}\hat{B}_{in} - \hat{\Xi}, \tag{A2}$$

which leads to the following covariance matrix for the output field as

$$C_B^{(out)}(\omega) = \langle \hat{B}^{(out)}(\omega)\hat{B}^{(out)}(\omega)^\dagger\rangle = [I + D^{1/2}(i\omega I + M)^{-1}D^{1/2}]\,\langle \hat{\Xi}(\omega)\hat{\Xi}^\dagger(-\omega)\rangle\,[I + D^{1/2}(i\omega I + M)^{-1}D^{1/2}]^\dagger. \tag{A3}$$

Equation (6) for MF can be solved to determine the MFs as well as the detunings, self-consistently. From now on, $\alpha_m \to |\alpha_m|e^{i\phi_m}$ and we drop the amplitude sign for brevity. Assuming the pump as $\Omega_0 e^{-i\phi_p}$, one can show the following relations:

$$\left(\frac{\alpha_1}{\alpha_3}\right)^2 = \frac{\gamma_3}{\gamma_1},\ \sin(\Phi_0) = \frac{\sqrt{\gamma_1\gamma_3}}{V_0\alpha_2^2},\ \Omega_0\sin(\Phi_p) = \alpha_2\big[1 + 2\alpha_2^2\alpha_1\alpha_3\sin(\Phi_0)\big],$$
$$\tilde{\Delta}_1 = \frac{\gamma_1}{\gamma_1+\gamma_3}(2\Delta_2 - \delta_D) + \frac{V_0\alpha_2^2}{\gamma_2(\gamma_1+\gamma_3)}\big[2(\gamma_1-\gamma_3) + 2\big(\gamma_1\alpha_1^2 - \gamma_3\alpha_3^2\big) + \big(\gamma_1\alpha_3^2 - \gamma_3\alpha_1^2\big)\big],$$
$$\tilde{\Delta}_3 = \frac{\gamma_3}{\gamma_1+\gamma_3}(2\Delta_2 - \delta_D) - \frac{V_0\alpha_2^2}{\gamma_2(\gamma_1+\gamma_3)}\big[2(\gamma_1-\gamma_3) + 2\big(\gamma_1\alpha_1^2 - \gamma_3\alpha_3^2\big) + \big(\gamma_1\alpha_3^2 - \gamma_3\alpha_1^2\big)\big], \tag{A4}$$

where $\Phi_0 = 2\phi_2 - \phi_1 - \phi_3$, $\Phi_p = \phi_p - \phi_2$.

Note that $\tilde{\Delta}_{1,3}$ are the renormalized detunings after extracting the LC oscillations. They therefore depend on other system parameters. From these equations it is clear that if $\gamma_1 = \gamma_3$ then the field amplitudes $\alpha_{1,3}$ and their renormalized detunings are the same. Moreover, $\tilde{\Delta}_{1,3}$ becomes MF independent, solely dependent on mode frequencies and the pump detuning. The difference between $\Delta_{1,3}$ in Eq. (4), i.e., the detuning in the laser rotating frame, and $\tilde{\Delta}_{1,3}$ in the above equation is the LC oscillations depicted in Fig. 5 of the main text. It is straightforward to check that the LC oscillations have the following frequency:

$$\tilde{\Delta}_{1,3} - \Delta_{1,3} = \pm\omega_{LC} = \pm\frac{\omega_3 - \omega_1}{2}. \tag{A5}$$

Note that the last equation respects the local U(1) symmetry of Eq. (11).

To study the squeezing it is often more suitable to investigate the behavior of field quadratures, related to field operators $\hat{B}$ via a unitary transformation U as $\hat{R} = [X_1, P_1, X_2, \ldots, P_3] = U\hat{B}$. The generalized quadratures of these modes are defined as follows:

$$\hat{X}_2(\theta_2) = \frac{\hat{A}_2 e^{i\theta_2} + \hat{A}_2^\dagger e^{-i\theta_2}}{\sqrt{2}}. \tag{A6}$$

The momentum quadratures are defined similarly. Their covariance matrix reads as

$$C_{XP}(\omega) = \langle \hat{R}(\omega)\hat{R}(\omega)^\dagger\rangle = UC_B(\omega)U^\dagger. \tag{A7}$$

For the three-mode cavity investigated in this work, we define new modes via a rotation of m_2 and symmetric and antisymmetric superpositions of the (also rotated) modes m_1, m_3 as

$$\hat{A}_2 = \hat{a}_2 e^{i\phi_2},\ \hat{A}_\pm = \frac{\alpha_1\hat{a}_1 e^{i\phi_1} \pm \alpha_3\hat{a}_3 e^{i\phi_3}}{\sqrt{\alpha_1^2 + \alpha_3^2}}. \tag{A8}$$

Note that $\hat{P}_-$ is the operator associated with the Goldstone mode G in Eq. (12).

A direct calculation of M for the XP operators indicates that for $(\theta_1 + \phi_1) = (\theta_3 + \phi_3)$, $M_{XP} = M_{4\times4} \bigoplus M_{2\times2}$, decoupling the dynamics of the m_2, m_+ modes from that of m_-. For $\theta_2 = -\phi_2$ the Bogoliubov matrix has the following form:

$$M_{XP} = \begin{bmatrix}
\frac{\Omega_0}{\alpha_2}\sin\phi_2 & 4V_0\alpha_1^2\cos\Phi_0 + \frac{\Omega_0}{\alpha_2}\cos\phi_2 & -2\sqrt{2}V_0\alpha_1\alpha_2\sin\Phi_0 & -2\sqrt{2}V_0\alpha_1\alpha_2\cos\Phi_0 & 0 & 0 \\
2V_0\alpha_2^2 - \frac{\Omega_0}{\alpha_2}\cos\phi_2 & 4V_0\alpha_1^2\sin\Phi_0 + \frac{\Omega_0}{\alpha_2}\sin\phi_2 & 2\sqrt{2}V_0\alpha_1\alpha_2(2+\cos\Phi_0) & -2\sqrt{2}V_0\alpha_1\alpha_2\sin\Phi_0 & 0 & 0 \\
2\sqrt{2}V_0\alpha_1\alpha_2\sin\Phi_0 & -2\sqrt{2}V_0\alpha_1\alpha_2\cos\Phi_0 & 0 & 2V_0\alpha_2^2\cos\Phi_0 & 0 & 0 \\
2\sqrt{2}V_0\alpha_1\alpha_2(2+\cos\Phi_0) & 2\sqrt{2}V_0\alpha_1\alpha_2\sin\Phi_0 & 6V_0\alpha_1^2 & -2V_0\alpha_2^2\sin\Phi_0 & 0 & 0 \\
0 & 0 & 0 & 0 & -2V_0\alpha_2^2\sin\Phi_0 & 0 \\
0 & 0 & 0 & 0 & -2V_0(\alpha_1^2 + \alpha_2^2\cos\Phi_0) & 0
\end{bmatrix}.$$

Clearly, M has a kernel along P_-, hence a gapless mode without any further dynamics.

The output spectrum of this mode can be directly obtained from $C_B^{(out)}(\omega)$ in Eq. (A3). For brevity we define a matrix N as

$$N = I + D^{1/2}(i\omega I + M)^{-1}D^{1/2}. \tag{A9}$$

From Eq. (A3) we get

$$C_{XP}^{(out)}(\omega) = U[N(U^\dagger U)\langle \Xi(\omega)\Xi^\dagger(-\omega)\rangle (U^\dagger U)N^\dagger]U^\dagger = (UNU^\dagger)[U\langle \Xi(\omega)\Xi^\dagger(-\omega)\rangle U^\dagger](UNU^\dagger)^\dagger, \tag{A10}$$

$$\begin{aligned} UNU^\dagger &= U[I + D^{1/2}(i\omega I + M)^{-1}D^{1/2}]U^\dagger = I + D^{1/2}U(i\omega I + M)^{-1}U^\dagger D^{1/2} \\ &= I + D^{1/2}[U(i\omega I + M)U^{-1}]^{-1}D^{1/2} = I + D^{1/2}(i\omega I + M_{XP})^{-1}D^{1/2}, \end{aligned} \tag{A11}$$

where $M_{XP} = UMU^{-1}$ is the Bogoliubov matrix of the generalized rotated quadratures. Note that in the above equation we implicitly assumed identical losses for all modes, i.e., $D^{1/2} = \sqrt{2\gamma_0}I$. Finally, the quadrature spectra of the m_- mode will be obtained as

$$\begin{aligned} S_{X_-}(\omega) &= \frac{1}{2}\left(\frac{(M_{XP_{55}} + 2\gamma_0)^2 + \omega^2}{M_{XP_{55}}^2 + \omega^2}\right) = \frac{1}{2}\left(\frac{\omega^2}{M_{XP_{55}}^2 + \omega^2}\right), \\ S_{P_-}(\omega) &= \frac{1}{2}\left(1 + \frac{4\gamma_0\left[\gamma_0\left(\omega^2 + M_{XP_{55}}^2 + M_{XP_{65}}^2\right) + M_{65}(2\gamma_0 + M_{55})\right]}{\omega^2\left(\omega^2 + M_{55}^2\right)}\right) = \frac{1}{2}\left(1 + \frac{4\gamma_0^2\left(\omega^2 + M_{XP_{55}}^2 + M_{XP_{65}}^2\right)}{\omega^2\left(\omega^2 + M_{XP_{55}}^2\right)}\right), \end{aligned} \tag{A12}$$

where we used the expression for Φ_0 from Eq. (A4) to simplify the final form of the spectrum. These two spectra have simple interpretations: First, they show that at the local oscillator frame $\langle \Delta^2 P_- \rangle$ diverges while $\langle \Delta^2 X_- \rangle$ vanishes. Moreover, for all frequencies the momentum quadrature is always above the standard quantum limit (SQL; $\geqslant 0.5$), and $S_{X_-} \leqslant 0.5$ below SQL, indicating the squeezing of this quadrature. Both quantities asymptotically approach SQL at large frequencies, as expected for the asymptotic vacuum noise.

APPENDIX B: WIGNER REPRESENTATION

The Wigner representation of the density matrix $\hat{\rho}$ in the complex plane can be derived from Eq. (3) by assigning c-numbers $\alpha_m^\pm$ for each degrees of freedom and using the following relations to replace the operator algebras with calculus ones on analytic function W. A detailed explanation of the Weyl transformation and Wigner function representation can be found in [43,44,58,59]. The basic tool for our purposes is the translation of operator products involving the density operator to c-number differential operators applied to the Wigner function as given by

$$\begin{aligned} \hat{a}_m\hat{\rho} &\to \left[\alpha_m^- + \frac{1}{2}\frac{\partial}{\partial\alpha_m^+}\right]W(\alpha_m^\pm;t), \\ \hat{a}_m^\dagger\hat{\rho} &\to \left(\alpha_m^+ - \frac{1}{2}\frac{\partial}{\partial\alpha_m^-}\right)W(\alpha_m^\pm;t), \end{aligned} \tag{B1}$$

$$\begin{aligned} \hat{\rho}\hat{a}_m &\to \left(\alpha_m^- - \frac{1}{2}\frac{\partial}{\partial\alpha_m^+}\right)W(\alpha_m^\pm;t), \\ \hat{\rho}\hat{a}_m^\dagger &\to \left(\alpha_m^+ + \frac{1}{2}\frac{\partial}{\partial\alpha_m^-}\right)W(\alpha_m^\pm;t). \end{aligned} \tag{B2}$$

Different terms of the master equation can be replaced with their equivalent form in terms of $W(\alpha_m^\pm)$, where $\alpha_m^\pm = (\alpha_m^\mp)^*$. For the bare-cavity dynamics (the commutator with $\omega_m\hat{a}_m^\dagger\hat{a}_m$ and the decay terms), we have

$$\frac{\partial}{\partial\alpha_m^-}[(i\omega_m + \gamma_m)\alpha_m^-] + \frac{\gamma_m}{2}\frac{\partial^2}{\partial\alpha_m^-\partial\alpha_m^+} + \text{c.c.}^+, \tag{B3}$$

where c.c.$^+$ in these equations represents the complex conjugate.

The self-phase modulation (SPM) as $\hat{a}_m^{\dagger 2}\hat{a}_m^2$ gets transformed to

$$\frac{\partial}{\partial\alpha_m^-}\left(\alpha_m^{-^2}\alpha_m^+ - \alpha_m^-\right) + \frac{1}{4}\frac{\partial^3}{\partial\alpha_m^-\partial^2\alpha_m^+}\alpha_m^+ + \text{c.c.}^+ \tag{B4}$$

The cross-phase modulation (XPM) $\hat{a}_m^\dagger\hat{a}_n^\dagger\hat{a}_n\hat{a}_m$, $n \neq m$ gives

$$\begin{aligned} &\frac{\partial}{\partial\alpha_m^-}\left(\alpha_m^-\alpha_n^-\alpha_n^+ - \frac{\alpha_m^-}{2}\right) + \frac{\partial}{\partial\alpha_n^-}\left(\alpha_n^-\alpha_m^-\alpha_m^+ - \frac{\alpha_n^-}{2}\right) \\ &\quad - \frac{\partial^3}{\partial\alpha_m^-\partial\alpha_m^+\partial\alpha_n^-}\left(\frac{\alpha_n^-}{2}\right) - \frac{\partial^3}{\partial\alpha_n^-\partial\alpha_n^+\partial\alpha_m^-}\left(\frac{\alpha_m^-}{2}\right) + \text{c.c.}^+ \end{aligned} \tag{B5}$$

And finally the exchange term as $\hat{a}_1^\dagger\hat{a}_3^\dagger\hat{a}_2^2 + \text{H.c.}$ gets the following form:

$$\begin{aligned} &\frac{\partial}{\partial\alpha_1^-}\left(\alpha_2^{-^2}\alpha_3^+\right) + \frac{\partial}{\partial\alpha_3^-}\left(\alpha_2^{-^2}\alpha_1^+\right) + \frac{\partial}{\partial\alpha_2^-}(2\alpha_1^-\alpha_3^-\alpha_2^+) + \text{c.c.}^+ \\ &\quad - \frac{\partial^3}{\partial\alpha_3^+\partial^2\alpha_2^-}\left(\frac{\alpha_1^-}{4}\right) - \frac{\partial^3}{\partial\alpha_1^-\partial\alpha_3^-\partial\alpha_2^+}\left(\frac{\alpha_2^-}{2}\right) \\ &\quad - \frac{\partial^3}{\partial\alpha_1^+\partial^2\alpha_2^-}\left(\frac{\alpha_3^-}{4}\right). \end{aligned}$$

When inserted into Eq. (3), one can determine the equation of motion for $W(\vec{\alpha};t)$ as

$$\frac{\partial}{\partial t}W(\alpha_m^\pm;t) = \mathcal{L}_W[W(\alpha_m^\pm;t)]. \tag{B6}$$

In the above equation $\mathcal{L}_W$ is a 3rd-order differential operator acting on the function $W(\vec{\alpha};t)$ and is equivalent to the

superoperator $\mathcal{L}$ acting on the density matrix $\hat{\rho}$. If the 3rd-order derivatives in $\mathcal{L}_W[.]$ are ignored, the resulting truncated Wigner function W turns into a Fokker-Planck equation with the following general form [45],

$$\frac{\partial}{\partial t}W(\vec{\alpha};t) \approx -\sum_m \partial_{\alpha_m}(A_m W) + \frac{1}{2}\sum_{m,m'}\partial^2_{\alpha_m\alpha_{m'}}(DD^T W), \tag{B7}$$

where A_m, D represent the drift and diffusion matrices in a stochastic process, respectively.

APPENDIX C: SUMMARY OF DPT IN A SINGLE-MODE CAVITY

To be able to directly compare some features of the multi-mode case with the single-mode cavity and shed some light on the connection between DPT and the Liouvillian gap closure here we summarize some results for a single-mode cavity case. More detailed information about various properties can be found in [11,24–26].

First-order DPT in a single-mode cavity

Starting from Eq. (6) we can drive the following equation for the mean photon number in the cavity mode as

$$V_0^2 n^3 + 2\Delta_0 V_0 n^2 + \left(\Delta_0^2 + 1\right)n = \Omega_0^2, \tag{C1}$$

where $n = |\alpha_2|^2$ is the photon number and all the rates are normalized to γ_0, as usual. This cubic equation can be solved exactly to give three values for n at each Ω_0. However, n being a real positive quantity imposes additional constraints for having a physical result. The discriminant of this cubic equation reads

$$\Delta = -V_0^2\left[27V_0^2\Omega_0^4 + 4V_0\Delta_0\Omega_0^2\left(9+\Delta_0^2\right) + 4\left(1+\Delta_0^2\right)^2\right]. \tag{C2}$$

For a repulsive interaction, i.e., $V_0 > 0$ and for a red-detuned coherent excitation $\Delta_0 \geqslant 0$, the discriminant $\Delta \leqslant 0$; hence the system always has a single real solution which is positive in this case $\Omega_0^2/V_0^2 \geqslant 0$. Following a dynamical stability analysis one can show that this solution is stable as well and, hence, it is the solution of the nonlinear cavity, as depicted in the phase diagram of Fig. 11(b). For a blue-detuned excitation $\Delta_0 < 0$, the same argument holds while the term in square brackets remains positive. For each detuning Δ_0, this puts an upper and lower bound on the pumping rate Ω_0. These are the boundaries between the yellow and orange regions in Fig. 11.

These two threshold pumping values lead to two different values for n in Eq. (C1), hence an abrupt change in the particle number as shown in Fig. 12. For pumping rates in between, Eq. (C2) leads to $\Delta < 0$; hence three different real solutions for the cubic Eq. (C1) exist. Moreover, these roots are positive; hence indeed they can be physical solutions for n. However, the dynamical stability analysis indicates that only particle numbers satisfying $(V_0 n + \Delta_0)(3V_0 n + \Delta_0) \geqslant 0$ are stable MF solutions. Since the upper and lower branches should remain continuous, and the intermediate solution for n within the multistability region is not stable, it could be left out from further considerations. That means the orange multistable region in Figs. 1(a), 1(b) is a bistable phase. Physically

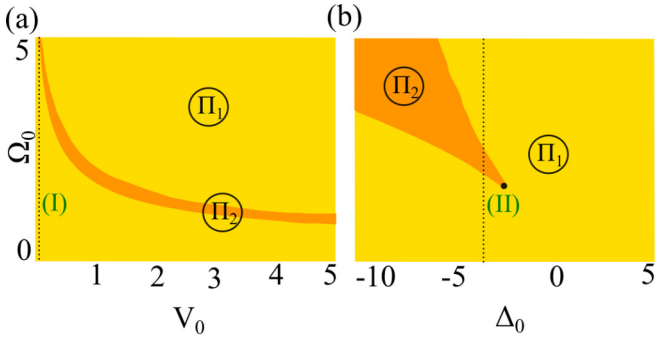

FIG. 11. MF dissipative phase diagram of a single-mode cavity as a function of (a) the interaction strength V_0 and (b) the laser detuning Δ_0. In each panel the yellow (Π_1) and orange (Π_2) regions correspond to one and two (bistability) stationary states for the pumped mode, respectively. In (a) the detuning is fixed at $\Delta_0 = -3$ and in (b) the interaction strength has the constant value $V_0 = 1$. The dotted vertical lines [labeled (I) and (II)] at $V_0 = 0.1$ and $\Delta_0 = -3$ indicate the cuts through the phase diagram studied in subsequent figures.

the instability of this solution is due to the divergence of parametrically generated side peaks shown in Figs. 13(a), 13(b). The Bogoliubov matrix M in this case has the following form:

$$M = \begin{bmatrix} -i(\Delta_0 - i\gamma_0) - i2V_0 n & -iV_0 n \\ iV_0 n & i(\Delta_0 + i\gamma_0) + i2V_0 n \end{bmatrix}. \tag{C3}$$

The eigenvalues of this matrix read as

$$\Lambda_\pm = -\gamma_0 \pm i\sqrt{(\Delta_0 + V_0 n)(\Delta_0 + 3V_0 n)}. \tag{C4}$$

From the above equation it is clear that for $(V_0 n + \Delta_0)(3V_0 n + \Delta_0) \geqslant 0$, the system is always stable as predicted before.

Figures 11(a), 11(b) show the MF-DPT of a single-mode cavity as a function of the interaction strength (V_0), the detuning (Δ_0), and the pumping rate (Ω_0). In each panel the yellow region shows the single-solution conditions while the orange ones correspond to the parameter ranges where the system has two different stable solutions (bistability region).

To better understand the system behavior in different phases we investigate the dependence of the cavity photon number on the pumping rate Ω_0, at a fixed detuning $\Delta_0 = -3$. The results obtained from the three different methods are compared in Figs. 12(a), 12(b) for weak [$V_0 = 0.1$ corresponding to the dotted line (I) in Fig. 1(a)] and strong interaction [$V_0 = 1$ corresponding to the dotted line (II) in Fig. 11(b)], respectively.

As can be seen, at low pumping rate and for both weak and strong interaction V_0, a displaced thermal state emerges inside the cavity. The effective temperature T increases with interaction strength starting from from 0 at $V_0 = 0$. Notice the larger deviation of $g^{(2)}(0)$ from unity when the interaction is increased as from Fig. 12(a) to 12(b). Within this range there is a good agreement between all three approaches.

As the pumping rate increases, however, the MF predicts a bistable behavior corresponding to a *first-order* phase transition, while both DM and SDE give a unique solution. In the MF picture, once the system reaches any of the stable

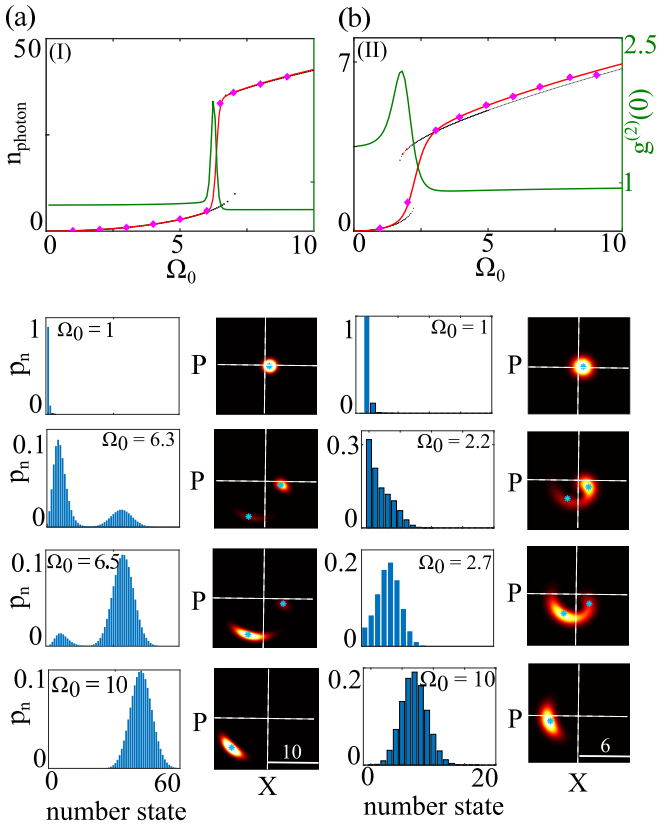

FIG. 12. Number of photons as a function of pumping rate (Ω_0) in a single-mode cavity with two-body interaction strength of (a) $V_0 = 0.1$ [dotted line (I) in Fig. 11(a)] and (b) $V_0 = 1$ [dotted line (II) in Fig. 11(b)]. The black dots show the mean-field result. The solid red line is the full density matrix result, and the purple diamonds represent the SDE results. The solid green line shows the intensity fluctuation $g^{(2)}(0)$. For each interaction strength the blue histograms show the number state occupation probability p_n at different pumping rates, before the bistability (first row), within the bistability (two middle rows), and after the bistability (last row). In each case, the color maps show the corresponding Wigner function distribution in the XP phase space. The white dashed lines show the axes ($X = 0, P = 0$) in that plane. Also the light blue stars in those panels indicate the predicted MFs. We use $\Delta_0 = -3$ in all cases.

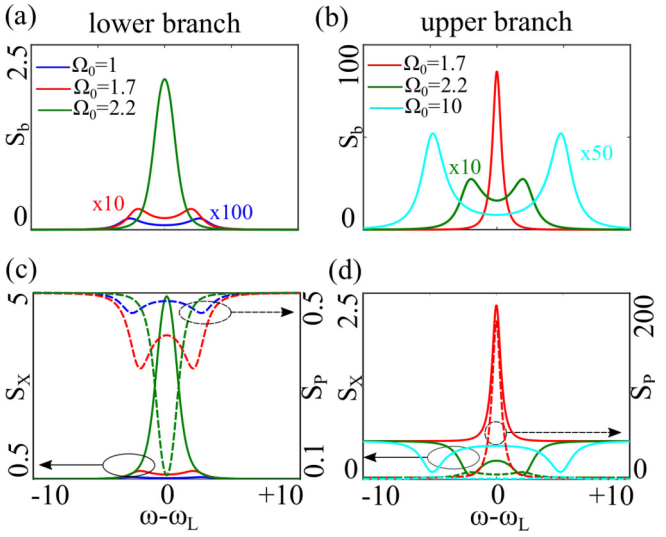

FIG. 13. Inelastic output intensity spectrum in the laser reference frame, i.e., $\omega - \omega_L$, when the pumping rate is increased on the MF (a) lower and (b) upper branches at $\Delta_0 = -3, V_0 = 1$. (c) and (d) show their corresponding X, P variance spectra calculated from Eq. (A11). Solid lines show X spectra and dashed lines are their corresponding P spectra.

stationary states the dynamics stops and the system stays there forever. Quantum mechanically, however, due to fluctuations these solutions are only *metastable* states and the system can switch between them. The signature of the quantum tunneling or switching between these states can be clearly observed in an increase of the intensity fluctuation $g^2(0)$ within the bistability region as depicted by the solid green line in Figs. 12(a), 12(b). Its deviation from unity outside the bistability range is another apparent deviation from MF.

To explore the tunneling phenomenon further, we compare the behavior of the system at weak [Fig. 12(a)] and strong [Fig. 12(b)] interaction as a function of the pumping rate. As can be seen by decreasing the interaction, the onset of bistability, the average number of cavity photons, and the difference between stable branches all increase. At weaker interactions, hence larger particle number, the fluctuations can be neglected and the quantum mechanical predictions approach the stable MF solutions. In the tunneling picture it can be understood as an increase of the barrier height at weaker interactions hence, rare tunneling events. This rate will be noticeably decreased upon increasing the interaction strength. The photon-number distribution within the bistability region and the corresponding Wigner function clarify this point better (middle panels of Fig. 12). At weaker interaction and within the bistability region, the number-state occupation probability p_n is bimodal and the peak intensities move toward higher photon number as the bistable phase is traversed ($\Omega_0 = 6.3, 6.5$). Similarly, the corresponding Wigner function has two well-separated local maxima in the XP plane around the MF stationary states that are depicted as black and white stars in each case. Upon increasing the interaction, both the occupation probability as well as the phase-space distribution show overlaps between the two states, which indicates that the tunneling can indeed be activated via fluctuations, as can be seen in Fig. 12 for $\Omega_0 = 2.2, 2.7$ at $V_0 = 1$.

If we increase the pumping rate even further, the system transitions to a unique-solution phase again (Π_1), as indicated by the singly peaked number-state occupation shown with the blue histograms at the bottom of Fig. 12. Unlike the low-power case however, the Wigner function has a banana-shaped distribution indicating the large asymmetry between X, P quadratures. In Appendix D one can find further discussion about the switching dynamics using one quantum Monte Carlo trajectory and prolonged correlation times within the bistability region.

Next, we investigate the quantum properties of the generated photons by calculating the output spectra of the case investigated in Fig. 12(b). The results are shown in Figs. 13(a), 13(b) obtained from the Bogoliubov matrix on the lower and upper MF branches, respectively. In this case, the parametric process leads to the generation of photon pairs

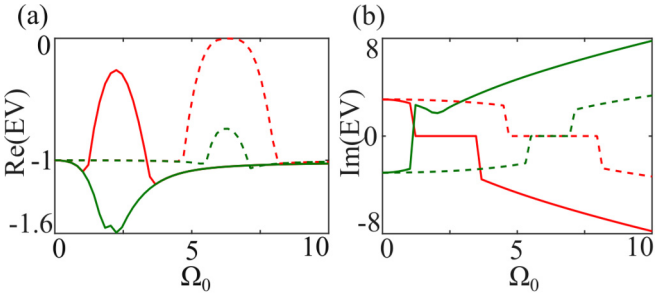

FIG. 14. (a) Real and (b) imaginary parts of the first three eigenvalues (EV) of the Liouvillian as a function of pumping rate Ω_0 in a single-mode cavity. The dashed and solid lines correspond to $V_0 = 0.1, 1$, respectively, at a fixed detuning of $\Delta_0 = -3$. All rates are in terms of γ_0.

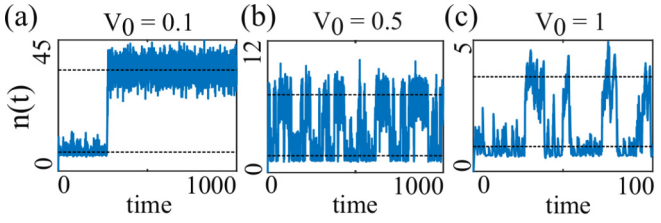

FIG. 15. Particle number as a function of time in a single-mode cavity at different interaction strength and within the MF bistability region for (a) $V_0 = 0.1$, $\Omega_0 = 6.5$, (b) $V_0 = 0.5$, $\Omega_0 = 3$, and (c) $V_0 = 1$, $\Omega_0 = 2.2$, determined from one trajectory of a quantum Monte Carlo simulation. In each panel the black dotted lines show the MF stationary states. The detuning is fixed at $\Delta_0 = -3$. The rates are in units of γ_0, and the time in units of γ_0^{-1}.

which appear as side peaks in the output intensity spectra, shown with the red and blue lines in Fig. 13(a). Notice that here we only focus on the correlation properties of $\hat{b}$, i.e., on the inelastic part of the spectrum. $S_b(\omega)$ is reminiscent of the Mollow triplet fluorescence spectrum of a coherently driven two-level system at high intensities.

Upon increasing the pumping rate (Ω_0) the effective detuning between the cavity mode and the laser frequency as well as the sideband spacing decrease. For spacing less than the linewidth γ_0, the double-peaked spectrum on the lower branch morphs to a single-peaked feature at the laser frequency ω_L, i.e., the solid green line in Fig. 13(a). Increasing the pumping rate further on the upper branch, the effective detuning and the sideband spacing increase again. This transition can be observed in Fig. 13(b) where the single-peaked spectrum at $\Omega_0 = 1.7$ (solid red line) turns into double-peaked spectra at higher pumping rates [green and cyan lines in Fig. 13(b)]. Unlike the lower branch, however, the sideband spacing monotonically increases with increasing the pumping rate and hence, no further MF bistability is observed. The corresponding output X, P quadratures, shown in Figs. 13(c), 13(d) for the lower and upper MF branches, respectively, indicate that there is always a partially squeezed quadrature (lines dip below SQL = 0.5). Aside from a finite region around the bistability threshold, the quadratures mostly satisfy $\langle \Delta^2 X \rangle \langle \Delta^2 P \rangle \approx 0.5$, hence, a minimum-uncertainty state as predicted by MF-Bogoliubov.

We consider an open system whose density-matrix dynamics are described via a Liouvillian $\mathcal{L}$ as $\dot{\hat{\rho}} = \mathcal{L}\hat{\rho}$. If there is a steady state $\hat{\rho}_{ss}$, it is a zero-eigenvalue eigenstate of Liouvillian: $\mathcal{L}\hat{\rho}_{ss} = 0$. Therefore, for a stable dynamics the real part of the spectrum of $\mathcal{L}$ is upper bounded at $\lambda = 0$.

Dissipative phase transitions typically go along with a closing of the dissipative gap, defined the $\max\{\mathrm{Re}(\lambda) : \lambda \neq 0, \lambda \in \mathrm{spec}(\mathcal{L})\}$. To illustrate the closure of the gap at the DPT threshold, we calculate the Liouvillian spectrum of the single-mode cavity discussed in the main text. Figures 14(a), 14(b) show the real and imaginary parts of the first three eigenvalues of $\mathcal{L}$ as a function of the pumping rate Ω_0 for $V_0 = 0.1$ (solid lines) and $V_0 = 1$ (dashed lines), respectively. The blue line shows the eigenvalue of the steady state, i.e., $\lambda = 0$. While far away from MF bistability regions the slowest timescale is set by the cavity decay rate, within the bistability range both interactions acquire a slower dynamics, set by an eigenvalue $\mathrm{Re}(\lambda_1) \gtrsim -1$. As can be seen in Fig. 14(b) within this range the imaginary part of this eigenvalue vanishes as expected from a slowed-down dynamics approaching the steady state.

Interestingly, in Fig. 14(a) the gap between λ_1 and zero decreases with decreasing the interaction, which implies a frozen dynamics around each MF steady state in the thermodynamic limit. This is also consistent with the tunneling picture and the switching times discussed in Fig. 12.

APPENDIX D: QUANTUM MONTE CARLO AND THE SWITCHING RATE IN FIRST-ORDER DPT

As discussed in the main text and described in Appendix C, in the thermodynamic limit the 1st-order PT is associated

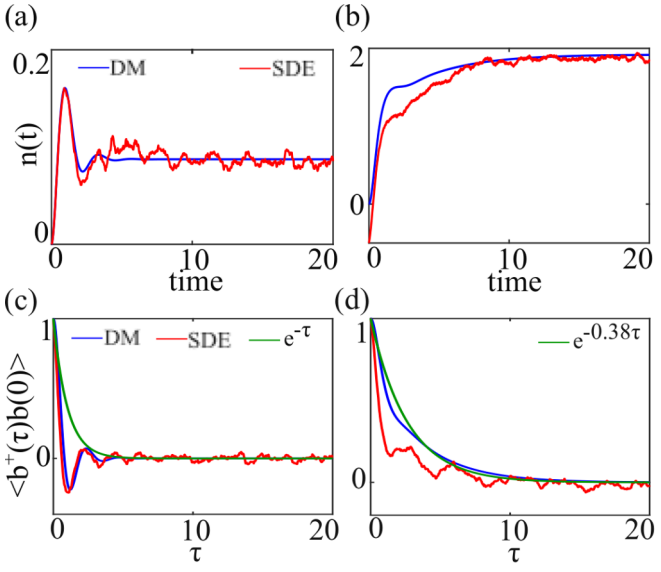

FIG. 16. Instantaneous photon number $n(t)$ in a single-mode cavity as a function of time (in units of γ_0^{-1}) for $V_0 = 1$, $\Delta_0 = -3$ and at (a) $\Omega_0 = 1$ and (b) $\Omega_0 = 2.2$. (c), (d) show the first-order correlation of the fluctuations as a function of delay τ. In each panel the solid blue line shows the density matrix (DM) calculations and the red line indicates the stochastic differential equation (SDE) results. The green lines in panels (c), (d) are the least-squares exponential fits to the correlation function tails.

with an abrupt jump at the critical parameter corresponding to multiple MFs (Fig. 15(a)). As the system departs from this limit, e.g., by increasing the interaction hence decreasing the particle number, the quantum jumps due to the fluctuations increase and hinder the MF multistability picture and lead to a unique solution when the system dynamics is treated fully quantum mechanically (Figs. 15(b) and 15(c)). The presence of these local minima, however, suggests that the quantum trajectory is most probable to be attracted to these stationary states.

This new timescale or the tunneling rate can be observed in any temporal dynamics of correlations of observables as well. Figures 16(a), 16(b) show the photon number relaxation toward the steady state at strong interaction $V_0 = 1$ for $\Omega_0 = 1, 2.2$, respectively. Figures 16(c), 16(d) show the behavior of their corresponding first-order correlation $g^{(1)}(\tau)$ as a function of the delay τ. For all cases the dynamics are determined via both full density matrix (DM in solid blue lines) as well as the stochastic differential equations (SDE in solid red lines). As can be seen the results from two approaches agree pretty well and they both predict different timescales in the unique [Figs. 16(a), 16(c)] and bistable [Figs. 16(b), 16(d)] region. While the former shows a fast relaxation toward the steady state with a rate of γ_0, the latter has a bimodal behavior. An exponential fit to the coherence tails, shown in solid green lines in Figs. 16(c), 16(d) indicates that the dynamics starts with a γ_0-scale behavior. Within the bistable region, however, the dynamics are slowed down by a factor of 2.5, related to the switching rate between two metastable solutions as predicted by the MF treatment.

[1] S. Sachdev, *Quantum Phase Transitions* (Cambridge University Press, UK, 2011).
[2] T. Vojta, Ann. Phys. **9**, 403 (2000).
[3] M. Greiner, O. Mandel, T. Esslinger, T. W. Haensch, and I. Bloch, Nature (London) **415**, 39 (2002).
[4] K. Baumann, C. Guerlin, F. Brennecke, and T. Esslinger, Nature (London) **464**, 1301 (2010).
[5] P. T. Brown, D. Mitra, E. Guardado-Sanchez, P. Schauss, S. S. Kondov, E. Khatami, T. Paiva, N. Trivedi, D. A. Huse, and W. S. Bakr, Science **357**, 1385 (2017).
[6] H. Deng, H. Haug, and Y. Yamamoto, Rev. Mod. Phys. **82**, 1489 (2010).
[7] I. Carusotto and C. Ciuti, Rev. Mod. Phys. **85**, 299 (2013).
[8] W. Bao, X. Liu, F. Xue, F. Zheng, R. Tao, S. Wang, Y. Xia, M. Zhao, J. Kim, S. Yang *et al.*, Proc. Natl. Acad. Sci. U.S.A. **116**, 20274 (2019).
[9] A. Amo, J. Lefrere, S. Pigeon, C. Adrados, C. Ciuti, I. Carusotto, R. Houdre, E. Giacobino, and A. Bramati, Nat. Phys. **5**, 805 (2009).
[10] G. Lerario, A. Fieramosca, F. Barachati, D. Ballarini, K. S. Daskalakis, L. Dominici, M. D. Giorgi, S. A. Maier, G. Gigli, S. Kena-Cohen *et al.*, Nat. Phys. **13**, 837 (2017).
[11] S. R. K. Rodriguez, W. Casteels, F. Storme, N. Carlon Zambon, I. Sagnes, L. Le Gratiet, E. Galopin, A. Lemaître, A. Amo, C. Ciuti, and J. Bloch, Phys. Rev. Lett. **118**, 247402 (2017).
[12] T. Fink, A. Schade, S. Hofling, C. Schneider, and A. Imamoglu, Nat. Phys. **14**, 365 (2018).
[13] I. Siddiqi, R. Vijay, F. Pierre, C. M. Wilson, L. Frunzio, M. Metcalfe, C. Rigetti, R. J. Schoelkopf, M. H. Devoret, D. Vion, and D. Esteve, Phys. Rev. Lett. **94**, 027005 (2005).
[14] Y. Yin, H. Wang, M. Mariantoni, R. C. Bialczak, R. Barends, Y. Chen, M. Lenander, E. Lucero, M. Neeley, A. D. O'Connell *et al.*, Phys. Rev. A **85**, 023826 (2012).
[15] T. Liu, Y. Zhang, B.-Q. Guo, C.-S. Yu, and W.-N. Zhang, Quantum Inf. Process. **16**, 209 (2017).
[16] M. Fitzpatrick, N. M. Sundaresan, A. C. Y. Li, J. Koch, and A. A. Houck, Phys. Rev. X **7**, 011016 (2017).
[17] M. Elliott, J. Joo, and E. Ginossar, New J. Phys. **20**, 023037 (2018).
[18] C. K. Andersen, A. Kamal, N. A. Masluk, I. M. Pop, A. Blais, and M. H. Devoret, Phys. Rev. Appl. **13**, 044017 (2020).
[19] S. Diehl, A. Tomadin, A. Micheli, R. Fazio, and P. Zoller, Phys. Rev. Lett. **105**, 015702 (2010).
[20] E. G. Dalla Torre, S. Diehl, M. D. Lukin, S. Sachdev, and P. Strack, Phys. Rev. A **87**, 023831 (2013).
[21] S. Morrison and A. S. Parkins, Phys. Rev. A **77**, 043810 (2008).
[22] E. M. Kessler, G. Giedke, A. Imamoglu, S. F. Yelin, M. D. Lukin, and J. I. Cirac, Phys. Rev. A **86**, 012116 (2012).
[23] J. Jin, A. Biella, O. Viyuela, C. Ciuti, R. Fazio, and D. Rossini, Phys. Rev. B **98**, 241108(R) (2018).
[24] W. Casteels, F. Storme, A. Le Boite, and C. Ciuti, Phys. Rev. A **93**, 033824 (2016).
[25] W. Casteels and M. Wouters, Phys. Rev. A **95**, 043833 (2017).
[26] W. Casteels, R. Fazio, and C. Ciuti, Phys. Rev. A **95**, 012128 (2017).
[27] W. Verstraelen, R. Rota, V. Savona, and M. Wouters, Phys. Rev. Research **2**, 022037 (2020).
[28] I. Carusotto and C. Ciuti, Phys. Rev. B **72**, 125335 (2005).
[29] P. D. Drummond and D. F. Walls, J. Phys. A: Math. Gen. **13**, 725 (1980).
[30] P. D. Drummond and D. F. Walls, Phys. Rev. A **23**, 2563 (1981).
[31] H. J. Carmichael, Phys. Rev. X **5**, 031028 (2015).
[32] N. Jia, N. Schine, A. Georgakopoulos, A. Ryou, L. W. Clark, A. Sommer, and J. Simon, Nat. Phys. **14**, 550 (2018).
[33] N. Schine, M. Chalupnik, T. Can, A. Gromov, and J. Simon, Nature (London) **565**, 173 (2019).
[34] L. W. Clark, N. Schine, C. Baum, N. Jia, and J. Simon, Nature (London) **582**, 41 (2020).
[35] E. Togan, H.-T. Lim, S. Faelt, W. Wegscheider, and A. Imamoglu, Phys. Rev. Lett. **121**, 227402 (2018).
[36] L. B. Tan, O. Cotlet, A. Bergschneider, R. Schmidt, P. Back, Y. Shimazaki, M. Kroner, and A. Imamoglu, Phys. Rev. X **10**, 021011 (2020).
[37] N. Materise, Springer Proc. Phys. **211**, 87 (2018).
[38] J. Klaers, J. Schmitt, F. Vewinger, and M. Weitz, Nature (London) **468**, 545 (2010).
[39] M. Wouters and I. Carusotto, Phys. Rev. B **75**, 075332 (2007).
[40] M. Wouters and I. Carusotto, Phys. Rev. A **76**, 043807 (2007).
[41] J. Leonard, A. Morales, P. Zupancic, T. Esslinger, and T. Donner, Nature (London) **543**, 87 (2017).

[42] M. Guo, F. Boettcher, J. Hertkorn, J.-N. Schmidt, M. Wenzel, H. P. Buechler, T. Langen, and T. Pfau, Nature (London) **574**, 386 (2019).

[43] C. Gardiner and P. Zoller, *Quantum Noise: A Handbook of Markovian and Non-Markovian Quantum Stochastic Methods with Applications to Quantum Optics* (Springer, New York, US, 2004).

[44] H. M. Wiseman and G. J. Milburn, *Quantum Measurement and Control* (Cambridge University Press, UK, 2011).

[45] B. Berg, L. I. Plimak, A. Polkovnikov, M. K. Olsen, M. Fleischhauer, and W. P. Schleich, Phys. Rev. A **80**, 033624 (2009).

[46] J. F. Corney and M. K. Olsen, Phys. Rev. A **91**, 023824 (2015).

[47] J. R. Johansson, P. D. Nation, and F. Nori, Comput. Phys. Commun. **183**, 1760 (2012).

[48] J. R. Johansson, P. D. Nation, and F. Nori, Comput. Phys. Commun. **184**, 1234 (2013).

[49] R. W. Boyd, *Nonlinear Optics* (Academic Press, USA, 2008).

[50] J. Qian, A. A. Clerk, K. Hammerer, and F. Marquardt, Phys. Rev. Lett. **109**, 253601 (2012).

[51] C.-K. Chan, T. E. Lee, and S. Gopalakrishnan, Phys. Rev. A **91**, 051601(R) (2015).

[52] M. Marconi, F. Raineri, A. Levenson, A. M. Yacomotti, J. Javaloyes, S. H. Pan, A. E. Amili, and Y. Fainman, Phys. Rev. Lett. **124**, 213602 (2020).

[53] H. Haken, *Laser Theory* (Springer-Verlag Berlin Heidelberg, Germany, 1984).

[54] V. D. Vaidya, Y. Guo, R. M. Kroeze, K. E. Ballantine, A. J. Kollar, J. Keeling, and B. L. Lev, Phys. Rev. X **8**, 011002 (2018).

[55] S. L. Braunstein and P. van Loock, Rev. Mod. Phys. **77**, 513 (2005).

[56] C. Santori, J. S. Pelc, R. G. Beausoleil, N. Tezak, R. Hamerly, and H. Mabuchi, Phys. Rev. Appl. **1**, 054005 (2014).

[57] H. Zhang, Q. Liu, X.-S. Xu, J. Xiong, A. Alsaedi, T. Hayat,, and F.-G. Deng, Phys. Rev. A **96**, 052330 (2017).

[58] H. Carmichael, *An Open Systems Approach to Quantum Optics* (Springer-Verlag Berlin Heidelberg, Germany, 1991).

[59] M. J. Steel, M. K. Olsen, L. I. Plimak, P. D. Drummond, S. M. Tan, M. J. Collett, D. F. Walls, and R. Graham, Phys. Rev. A **58**, 4824 (1998).